Site-Selective Modification of Metallic Nanoparticles

Journal:	*ChemComm*
Manuscript ID	CC-FEA-06-2022-003603.R1
Article Type:	Feature Article

ChemComm

ARTICLE

Site-Selective Modification of Metallic Nanoparticles

Khoi Nguyen L. Hoang,‡ Sophia M. McClain,‡ Sean M. Meyer, Catherine A. Jalomo, Nathan B. Forney, Catherine J. Murphy*

Surface patterning of inorganic nanoparticles through site-selective functionalization with mixed ligand shells or additional inorganic material is an intriguing approach to developing tailored nanomaterials with potentially novel and/or multifunctional properties. The unique physicochemical properties of such nanoparticles are likely to impact their behavior and functionality in biological environments, catalytic systems, and electronics applications, making it vital to understand how we can achieve and characterize such regioselective surface functionalization. This Feature Article will review methods by which chemists have selectively modified the surface of colloidal nanoparticles to obtain both two-sided Janus particles and nanoparticles with patchy or stripey mixed-ligand shells, as well as to achieve directed growth of mesoporous oxide materials and metals onto existing nanoparticle templates in a spatially and compositionally controlled manner. The advantages and drawbacks of various techniques used to characterize the regiospecificity of anisotropic surface coatings are discussed, as well as areas for improvement, and future directions for this field.

1. Introduction

Advancements in the synthesis and characterization of structures on the nanoscale have been fundamental to the progression of technologies in fields ranging from electronics to healthcare. Transistors used in the first computer processors in the 1960s had a gate length of approximately 10 μm; however, with improvements in lithography and epitaxy techniques, transistor dimensions have since been reduced to just single digit nanometers, affording improved performance and reduced production cost by allowing more transistors to be packed on a single chip **(Figure 1A).** [1–5] Decreasing the grain size of drug powders from the microscale into the nanoscale regime has afforded medicinal benefits by enhancing bioavailability through improved drug dissolution rates which scale linearly with available surface area.[6] Delivery of small-molecule drugs can also be improved through incorporation into nanoparticle systems. One benchmark example is the cancer therapeutic Abraxane® which comprises a cross-linked shell of albumin proteins surrounding a hydrophobic core containing the active paclitaxel drug molecules (**Figure 1B)**. On its own, paclitaxel requires formulation in a toxic solvent system which forms drug-sequestering micelles. However, Abraxane® is stable in a simple saline solution and undergoes a dynamic dissolution process in the bloodstream to release smaller albumin-paclitaxel complexes, simultaneously decreasing toxicity and improving bioavailability compared to the conventional

formulation.[7] Abraxane® also leverages the natural albumin transcytosis pathway to enhance penetration of paclitaxel molecules into tumor cells.[8]

The exact size within the nanoscale regime has also been shown to impact particle internalization pathways and uptake efficiency.[9] While factors such as cell type and particle material could also play a role, studies investigating a variety of particle/cell combinations have shown that the highest degree of internalization by cells is achieved for particles ~50 nm in diameter,[10–13] although a few reports suggest uptake is optimal for ~100 nm objects.[14,15] Particles in this size range are typically internalized by caveolin- or clathrin-mediated endocytosis,
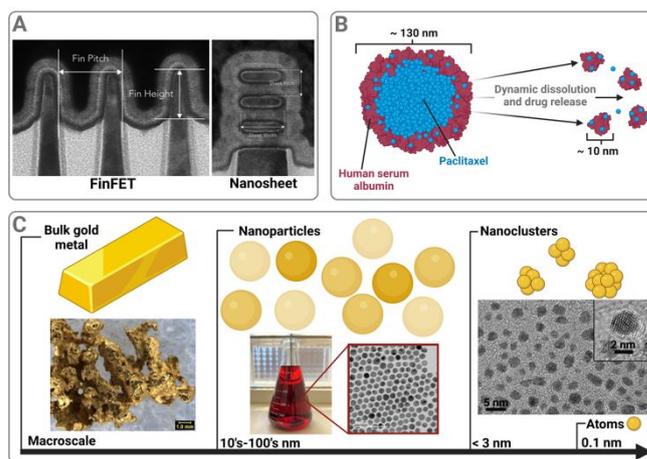

Figure 1. Examples of nanoscale features. **(A)** TEM cross-sections of FinFET (left) and nanosheet (right) transistors. Reproduced with permission from ref. 5, Copyright 2018 Elsevier. **(B)** Illustration of an Abraxane® nanoparticle comprising human serum albumin (maroon) and paclitaxel (blue), **(C)** Length scale along which gold exhibits changing properties. Photograph of gold nugget adapted with permission from ref. 17, Copyright 2019 Elsevier. TEM image of gold nanoclusters adapted with permission from ref. 22, Copyright 2019 Springer Nature. Made with Biorender.com.

while particles of diameter >500 nm are taken up via

Department of Chemistry, University of Illinois Urbana-Champaign, 600 South Mathews Avenue, Urbana, Illinois 61801, United States
*Email: murphycj@illinois.edu
‡: these authors contributed equally to this work.

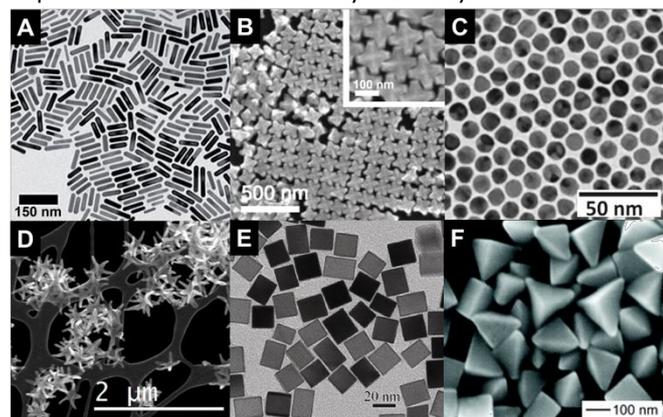phagocytosis; smaller particles of diameter <10 nm may be able to penetrate the membrane bilayer directly.[16]

Figure 2. Selection of metal nanoparticle shapes highlighting the control chemists now have to produce well-defined structures. **(A)** Transmission electron microscopy of Au nanorods. Adapted with permission from ref. 23, Copyright 2016 Royal Society of Chemistry. **(B)** Scanning electron microscopy of AuPd octopods. Adapted with permission from ref. 24, Copyright 2019 Royal Society of Chemistry. **(C)** Transmission electron microscopy of Au nanospheres. Adapted with permission from ref. 25, Copyright 2016 American Chemical Society. **(D)** High-angle annular dark-field scanning transmission electron microscopy of of AuCu nanostars. Adapted with permission from ref. 26, Copyright 2019 American Chemical Society. **(E)** Transmission electron microscopy of Pd nanocubes. Adapted with permission from ref. 27, Copyright 2017 Springer Nature. **(F)** Scanning electron microscopy of Ag right bipyramids. Adapted with permission from ref. 28, Copyright 2006 American Chemical Society.

When metals are scaled down from bulk materials[17] to particles on the order of 10s-100s nm, new size and shape dependent optical properties emerge.[18,19] Furthermore, even smaller molecular-sized gold clusters **(Figure 1C)** have been shown to display catalytic properties not observed in larger nanoparticles or bulk material. [20–22] The size and shape of these nanoscale structures are relatively easy to visualize by electron microscopy techniques and over the years a wide variety of nanoparticle morphologies have become accessible, a selection of which are displayed in **Figure 2**. [23–28] For nanoparticles made of crystalline inorganic materials, crystal structures of distinct facets can be identified and characterized using electron
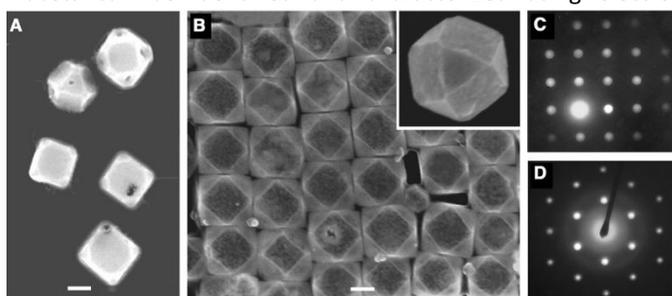

Figure 3. Electron microscopic characterization of nanocrystal shape and facets **(A,B)** SEM images of silver nanocubes after reaction with **(A)** 0.3 ml and **(B)** 1.5 ml of aqueous HAuCl4 solution (1 mM). **(C** and **D)** Electron diffraction patterns of two resultant gold nanoboxes with their square {100} facets and triangular {111} facets oriented perpendicular to the electron beam, respectively. Scale bars 100 nm. Reproduced with permission from ref. 29, Copyright 2002 The American Association for the Advancement of Science.

diffraction**(Figure 3)**.[29] However, it is much more difficult to image the nature of the surface chemistry on these structures (stabilizing ligands, terminal hydroxyl groups, etc.) and to assess the spatial distribution of such chemical moieties.

At this stage in the field of metal nanomaterials synthesis, shape and facet control of the final structures is becoming more routine. Thermodynamic arguments regarding {111} or {100}

facet stabilization with ligands such as halides allow for some predictability at the front end of synthesis.[30–32] Yet the field of nanomaterials synthesis is still not at the level of small-molecule organic synthesis, in which individual atoms of a molecule can be selectively reacted to produce new compounds. The analogue of site-specific reactivity in the world of nanomaterials would correspond to selective functionalization of particular facets on a nanocrystal, which has seen some success.[33,34]

This Feature Article will focus on the design and characterization aspects of how chemists can selectively modify different regions of nanoscale objects in colloidal solution. The ability to do so, routinely, would open up the synthetic capability and enable an exponential increase in the materials available for applications in catalysis,[35,36] biosensing,[37–39] nano-enabled drug delivery,[40,41] metamaterials,[42] and more. In the first section, we discuss and compare different site-selective modification methods that allow for the synthesis of Janus particles, which are colloidal particles with two distinct surface chemistry compositions. We then focus on different synthetic approaches available to selectively grow inorganic patches on inorganic nanoparticles, mainly silica on either the ends or sides of anisotropic gold nanorods. We also dedicate a section to methods which incorporate additional metal material onto pre-existing metal nanoparticles in a spatially and compositionally controlled manner. In later sections, we highlight the power of site-selective surface functionalization in mediating nanoparticle assemblies before discussing particles with molecular stripes, patches or altered ligand densities on their surface in more detail. The last section will evaluate the present state of the field and discuss opportunities for further developments in both synthetic methodologies and characterization techniques to prepare nanomaterials with precise biophysiochemical properties.

2. Janus Particles

Janus particles, termed after the Roman god of transitions and dualities, are among the earliest demonstrations of anisotropic nanoparticles, displaying two distinct chemical compositions on the surface of a single nanoparticle.[43,44] Typically, in order to obtain such bilateral surface chemistry, a boundary must be defined. This can be achieved by immobilizing particles on a substrate and depositing a secondary material or ligand on the exposed surface. Alternatively, nanoparticles' surface chemistry can be modified by incorporating two core materials, rather than one, allowing each region to attract distinct ligands. The first Janus particle synthesis was reported by Casagrande *et al*. in which they prepared 50 μm Janus glass beads by temporarily coating one hemisphere with an adhesive mask in order to preferentially treat the free hemisphere with a hydrophobic monolayer of octadecyltrichlorosilane.[45] The distinct properties of the two resultant surface chemistries were observed when the glass spheres aligned at the water-oil interface according to their newly formed hydrophobic and hydrophilic hemispheres.[46] Since this pioneering work, researchers have improved and expanded upon the synthetic methods available for the production of Janus particles through surface

modification, as well as developed approaches to form heterodimer Janus particles comprising multiple distinct core materials.[47]

Figure 4. Approaches to Janus particle synthesis. **(A)** Charged nanospheres with fluorescent (red) and nonfluorescent (yellow) hemispheres. Reproduced with permission from ref. 49, Copyright 2006 American Chemical Society. **(B)** Diagram of Langmuir-Blodgett technique used to make nonsymmetrical polymeric microspheres. Reproduced with permission from ref. 51, Copyright 2000 American Chemical Society. **(C)** Schematic of wax-silica particle colloidosomes used as substrates for particle masking. Reproduced with permission from ref. 52, Copyright 2006 American Chemical Society. **(D)** Two-drug PLGA-Janus nanoparticles prepared with fluidic nanoprecipitation. Reproduced with permission from ref 57, Copyright 2012 American Society of Chemistry.

As demonstrated in the foundational work, Janus particles can be formed by using masking techniques to protect one region of the particles while the other is modified. One method by which to carry out this masking technique is through the immobilization of particles onto a substrate.[48] This approach typically involves the following steps: fixation of particles onto a glass slide, chemical modification, and removal of particles from the substrate with ethanol or dilute acid. Granick and co-workers used this approach to prepare two-toned nanoparticles with hemispheres possessing distinct optical and electrostatic properties. They achieved this by first depositing a layer of fluorescent, anionic 1 µm polystyrene (PS)-carboxylate particles onto a glass surface. The unprotected surface was then coated with a 15-nm layer of gold using electron-beam deposition to make it non-fluorescent, and functionalized with N,N,N-trimethyl(11-mercaptoundecyl)ammonium chloride, to impart positive surface charge **(Figure 4A)**.[49] Solomon and co-workers used a similar approach, but added a 2.5 nm layer of titanium to assist with adherence of the gold layer to PS particles. This study revealed that surface thiol ligands of varying lengths and gold layers of different thicknesses could control the probability of particle self-assembly as well as their arrangement. Nonspecific interactions can also occur between Janus particles, which increase with increasing gold layer's thickness.[50] It is not yet understood whether longer self-assembled monolayer (SAM) ligands would counteract this phenomenon or the extent of nonspecific interactions between Janus particles that are not masked by a metal layer. The Langmuir-Blodgett (L-B) technique has also been used to prepare nonsymmetrical surface chemistries on microspheres by depositing a L-B derived polymer film onto a substrate-supported monolayer of microspheres. In one example of this approach, amino-activated polymeric microspheres were dispersed into a monolayer using butanol spread on a water surface, then transferred to a glass substrate. Next, a monolayer of terpolymerized nitrophenyl acrylate, p-nitrophenol, and N-octadecyl acrylamide was formed on the water surface and picked up with the particle-coated glass substrate, depositing a polymer layer on one hemisphere of the particles (**Figure 4B**). This process can then be repeated to deposit multiple coating layers on the particle surface. The L-B technique allows for the incorporation of two surface chemistries on microspheres without using a metal masking layer.[51]

One drawback of immobilization techniques is that they significantly limit the number of particles being treated at once due to only a single layer of particles being exposed. Procedures utilizing emulsions greatly improved the scale of Janus particle synthesis by increasing the area of interface for masking. One such procedure, developed by Granick and colleagues, utilized the liquid-solid interface of water and oil solidified into wax to create Janus particles in large quantities. An emulsion of molten wax and silica particles suspended in water was formed at high temperature and then cooled, solidifying the wax and locking the silica particles in place at the wax-water interface (**Figure 4C**). From here, the exposed surface of the particles was chemically modified with positively-charged fluorescent-labelled (aminopropyl)triethoxysilane. The wax cores were then
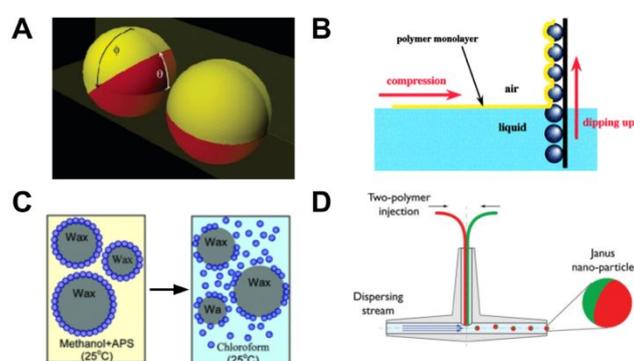
dissolved in chloroform to release the particles trapped at the surface, allowing the previously protected hemisphere to react with n-octadecanetrichlorosilane. Modifying each hemisphere separately resulted in Janus spheres with one hydrophobic side and one hydrophilic side.[52] Although beneficial for increasing production throughput, this approach is mainly limited to spherical particles. Additionally, hemisphere boundaries may not be as well-defined compared to immobilization methods because of fluctuations at the liquid-solid interface.

In addition to anisotropic surface functionalization, heterostructured Janus particles possessing two distinct core materials can also be synthesized.[47] Gu et al. prepared Fe_3O_4–Ag heterodimers by dispersing Fe_3O_4 nanoparticles (NPs) in organic solvent and then creating an emulsion with an aqueous solution of $AgNO_3$. Self-assembly of the Fe_3O_4 NPs at the water-solvent interfaces of the emulsion then allowed for the heterogeneous deposition of a Ag domain onto the water-exposed hemisphere of the particles. The Fe_3O_4 region of the resulting particles could then selectively react with a diol, while the Ag region reacted preferentially with a thiol-terminated fluorescent porphyrin to achieve two distinct ligand environments on the particle surface.[53] Furthermore, Xu et al. have shown that the interfacial energy of $Au-Cu_2O$ NPs can be tuned to achieve a transition from core-shell to Janus nanostructures by modifying the initial Au seeds with varying amounts of a strong thiol ligand, 5-amino-2-mercaptobenzimi-dazole (AMBI). Unlike weak-binding ligands such as citrate or cetyltrimethylammonium bromide (CTAB), it is expected that not all AMBI would desorb during Cu_2O deposition. The remaining AMBI patches then act as defects which weaken $Au-Cu_2O$ binding and disrupt lattice matching causing interfacial strain. This in turn leads to a series of $Au-Cu_2O$ nanoparticles with varying Janus degrees based on the amount of AMBI added to the system. They also determined that the Janus architecture affords enhanced charge separation, demonstrating a photocurrent 5 times greater than the core-shell structure and 10 times greater than neat Cu_2O cubes, showing the great potential for these Janus structures in photocatalytic applications.[54] The unique dual component architecture of Janus nanostructures has also been leveraged to afford multifunctional properties for various biological applications. Li et al. developed a Janus particle system for wound infiltration and coagulation by combining a $CaCO_3$ domain to serve as a nanomotor and a microporous starch domain which could be loaded with a coagulant such as thrombin.[55] The use of Janus particles for tumor growth inhibition has also been explored by employing Janus gold nanostar-iron oxide nanoparticles to induce a combination of photothermia and magnetic-hyperthermia in cancer cells.[56] Bipolymeric nanoparticles form another class of Janus particles which can be applied as drug delivery vehicles when surface modifications alone are inadequate. Smith and co-workers used a fluidic nanoprecipitation system to produce biocompatible poly(lactic-co-glycolic acid) (PLGA) particles comprised of one hydrophilic (PLGA-COOH) doxorubicin-containing hemisphere and one hydrophobic (PLGA) paclitaxel-containing hemisphere (**Figure 4D**).[57] Overall, advancements in the scale and diversity of Janus

particle synthesis have provided more control over particle properties and opened the door for exploration into more complex systems.

3. Inorganic Patches on Inorganic Nanoparticles

3.1. Site-Selective Growth of Silica on Gold Nanorods and Other Anisotropic Gold Particles

Combining multiple inorganic components into a single nanoparticle platform is a convenient way to impart these systems with multifunctionality and expand their application scope.[58] Many methods exist to combine different inorganic components, usually by growing an isotropic shell of one material around a second core material to form core-shell nanoparticles.[59] Here we explore several examples of unconventional marriages between different inorganic nanomaterials, using plasmonic metals as a foundation.

Shrinking gold crystals to the nanoscale unlocks a strong interaction with light that can be leveraged for a litany of applications. The conduction band electrons can oscillate in unison with the electric field vector of incident light at the proper frequency. This excitation, called a plasmon, generates strong electric fields at the surface of gold structures, especially if the particles possess areas of high curvature or sharp/curved tips. Using site-selective growth of porous oxides and other materials onto the surface of anisotropic nanoparticles such as gold nanorods (AuNRs) is a powerful way to impart functionality specifically to the active sharp tip. AuNRs are common multicomponent platforms for this due to their intrinsic anisotropy available via the shape itself and the presence of a surfactant bilayer on their surface. AuNRs are grown in a solution of CTAB, a quaternary ammonium surfactant, which imparts a large positive surface charge density and coats the rods in a bilayer of CTAB molecules.[60] The resulting anisotropic shape possesses two distinct regions in the sides and tips, both of which can be targeted independently.[61] The tips of the rod contain high surface energy facets, such as {111}, and have higher surface curvature compared to the sides and therefore under the correct conditions anisotropic inorganic coatings can be deposited. Finally, the curvature at the tips changes the packing density of the CTAB bilayer to promote a difference in surface chemistry between the two regions, a phenomenon that we will explore more in depth vide infra. The most prominent example of site-specific chemistry for these anisotropic nanomaterials is the deposition of mesoporous oxide materials on either the tips, sides, or all around the surface of a AuNR.[62] This way the active portions of a plasmonic nanorod can be utilized over the less active sides as it is well-known that under longitudinal excitation, the ends of AuNRs show far greater local electric fields than the sides.[63] For instance, by selectively attaching silica to just the tips of nanorods, we have shown the limit of detection for Raman-active analytes that bind to the silica can be decreased, compared to all-the-way-around silica shells, demonstrating the potential for site-selective silica deposition to enhance SERS-based molecular sensing applications.[64] Additionally, multiple

shapes can be used as platforms for selective growth in a plethora of ways.

Mesoporous oxide growth is found through the base and acid-catalyzed hydrolysis and condensation in solution in the presence of colloidal AuNRs. The dynamic nature of the CTAB bilayer means controlling the excess CTAB concentration in solution can change both the partitioning of available hydrolyzed precursors between the CTAB bilayers on the rods and the CTAB micelles in solution,[65] and the density of the CTAB bilayer on the surface.[66] In the case of mesoporous silica, tetraethylorthosilicate (TEOS) is the silica-containing precursor and under basic conditions negatively charged silanol groups of the TEOS molecules begin to form oligomers and deposit onto positively charged CTAB containing surfaces (AuNRs or micelles). Mixing an excess of TEOS with AuNRs in a dilute CTAB solution yields fully coated mesoporous silica coatings, as shown by Gorelikov et al.,[67] and expanded on by Abadeer et al.[65] that adding CTAB slightly beyond the critical micelle concentration (cmc, 1 mM) creates more micelles for TEOS oligomers to condense on, thus giving smaller shells to the AuNRs. Interestingly, both raising and lowering the CTAB concentration far from the cmc can induce anisotropic growth of silica on the surface of the AuNRs. We have shown that using a CTAB concentration below the cmc (0.7 – 0.8 mM) along with lowering the TEOS concentration grows silica shells just on the tips of the rods (**Figure 5A,B**),[68] while Zhu et al.[69] have shown that by increasing the CTAB concentration far beyond the cmc tip-directed growth can also be achieved under similar TEOS concentration as below the cmc**.**

This phenomenon that depends on the variable CTAB concentration has been noted by several authors and can be explained via the interplay of hydrolysis and condensation rates of TEOS and the change in CTAB bilayer composition.[70] The hydrolysis rate is rapid due to the predominantly aqueous environment, so adjusting the CTAB concentration changes the rate of condensation tremendously.[71,72] At low CTAB concentrations, there is minimal CTAB surrounding the AuNRs so the barrier for nucleation becomes low and slow nucleation leads to the high energy tips becoming coated first. Conversely at high CTAB concentration the barrier for nucleation around the sides of the AuNR becomes too great, so if there is enough TEOS to compensate for the increased micellar concentration, tip growth is favored. In principle, one could alter the rate of condensation and the energy barrier to growth on the gold surface through other means, and Rowe et al. discovered that doping in different amounts of alcohol to the aqueous system, the shells could be isolated to the tips or the entire rod.[73] The ideal concentrations of CTAB and TEOS which result in anisotropic shapes is also dependent on the gold nanorod size and concentration where larger aspect ratio rods have much better tip-directed growth but result in poor colloidal stability, as shown by Adelt et al.[71] There are many confounding factors in the anisotropic growth of silica on the surface, but it is clearly dependent on the rate of the TEOS condensation and the presence of high curvature regions like a sharp tip.

It is also possible to grow coatings just on the sides of the AuNR, albeit the process is less frequently seen in the literature.

Wang et al. originally proposed that introducing thiolated polyethylene glycol (PEG-SH) to the AuNR solution would selectively functionalize the tips of the AuNRs and block the growth of silica.[62,69] This technique, while initially useful for many varieties of nanostructures, was found to be difficult to reproduce. Upon reviewing this method, we learned that the disulfide, or oxidation product of the PEG-SH, was responsible for the anisotropic coatings due to the increased steric hindrance of the thiol moiety in the disulfide.[74] DNA has also been used to site-selectively grow silica coatings on rod-shaped upconversion nanoparticles (UCNPs), as shown by Ren et al. In this system, the phosphodiester bond in the backbone of DNA preferentially replaces the surfactant molecules on the (001) facets of UCNPs, preventing the growth of silica shell on the tips of the rods. The authors also found that UCNPs with anisotropic silica coating exhibit higher cellular uptake compared to isotropic silica coating.[75]

3.2. Other Site-Selective Coatings on Plasmonic Nanoparticles

In principle, the concepts described in the preceding section could be applied to other hydrolysis-condensation reactions involving precursors that can attach via CTAB headgroups to particle surfaces, or other anisotropic structures with widely varying curvature regions. Titanium dioxide was shown by Wu et al. to be able to deposit on the tips selectively at similar CTAB concentrations to the respective silica coatings.[76] Interestingly, they also altered the chain length of the surfactant molecule to tune the packing density of the surfactant bilayer and show that larger chain length blocks the deposition of titania only on the tips. Smaller chain lengths lead to higher yields of tip-selective titania growth presumably because the lower hydrophobic interaction between surfactant molecules loosens the bilayer at the tips for easier access. Growing ceria only on the tips of a AuNR is also possible, as shown by Jia et al., even though ceria requires a titanium catalyst for rapid oxidation.[77] The titanium precursor was attached to the surface of the particle and a similar CTAB method was used to introduce the cerium ions to the tips of the rods for nucleation and growth.

Metal organic frameworks can also grow selectively at the tips in similar conditions showing this platform is applicable to materials not grown by hydrolysis and condensation reactions.[78] In addition to AuNRs, both cubes and bipyramids
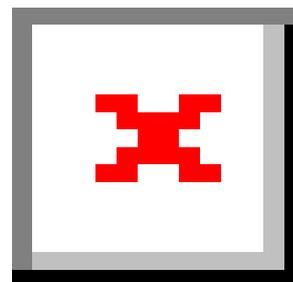
Figure 5. Examples demonstrating the site-selective growth of silica on anisotropic gold nanoparticles. **(A, B)** TEM micrographs of fully silica-coated gold nanorods and end-capped silica gold nanorods, respectively. Adapted from ref. 68, Copyright 2022 Royal Society of Chemistry. **(C)** Illustrations and TEM micrographs showing the shift in silica shell coating morphology on gold nanobipyramids as the volume of 0.1M CTAB added to the reaction mixture increases. Adapted with permission from ref. 69, Copyright 2017 John Wiley and Sons.

are ideal candidates for site-selective shell growth. As proven by Hong *et al.*[79] a semiconducting copper oxide coating can be selectively isolated to the cube corners or excluded from the corners depending on the surface coating, and Zhu *et al.*[69] showed that the exact procedure for AuNRs can be applied for nanobipyramids to grow porous silica shells on the tips **(Figure 5C)**.

3.3. Heterostructured Nanoparticles with Multiple Metal-Based Domains

Figure 7. The scanning-probe block copolymer lithography (SPBCL)-mediated synthesis of multimetallic nanoparticles and a five-element library of unary and multimetallic nanoparticles made via this technique. **(A)** Scheme depicting the process: A polymer loaded with metal ion precursor is deposited onto a substrate in the shape of a hemispherical dome via dip-pen nanolithography. After two-step thermal annealing, the metal precursors are aggregated and reduced, the polymer is decomposed, and individual nanoparticles result from each dome feature. The interwoven patterns in the NP schemes are only meant to indicate the alloying of the elements and not the actual atomic structure. **(B)** Unary NPs (top row is a color-coded diagram of the anticipated result; bottom row is each particle, as characterized by EDS mapping). **(C)** Binary NPs consisting of every two-element combination of the five metals; the alloy versus phase-segregated state was consistent with the bulk phase diagrams for each two-element combination. **(D)** Ternary NPs consisting of every three-element combination of the five metals; the prediction of alloy versus phase-segregated state was based on the miscibility of the three components, extracted from the binary data. **(E)** Quaternary NPs consisting of every four-element combination of the five metals; the prediction of alloy versus phase-segregated state was based on the miscibility of the four components, extracted from the binary and ternary data. **(F)** A quinary NP consisting of a combination of Au, Ag, Cu, Co, and Ni; the prediction of alloy versus phase-segregated state was based on all of the previous data for the unary through quaternary systems. Reproduced with permission from ref. 80, Copyright 2016 The American Association for the Advancement of Science.

Engineering multiple metals into a single nanosized entity is a challenging but ideal way to enable different functionalities to enable different functionalities to colloidal NPs. Careful design and synthesis of the placement of metal domains with respect to each other is key to efficient application use. Mirkin and co-workers have shown tremendous capability to make NPs with complex metallic domain architecture from single interface Janus-type particles to five interfaces between different metal phases.[80] To do so, a specially designed tip-probe setup wherein metal-ion-containing inks are deposited in nano-sized fashion in an array and thermally annealed to produce multimetallic nanoparticles was used **(Figure 6)**. This technique has been applied to Au, Ag, Cu, Co, Ni, Sn, and Pd domain particles, with the ability to combine any number of the aforementioned metals into a single particle.[81] It is possible to engineer various positions of the phases based on the composition and annealing time into multimetallic particles with various metallic junctions

Figure 6. Synthesis and characterization of heterostructured nanorods. **(A)** Schematic showing the reaction setup and injection sequence that incrementally transform G-1, $Cu_{1.8}S$, into G-6, $ZnS-CuInS_2-CuGaS_2-CoS-(CdS-Cu_{1.8}S)$. **(B)** STEM–EDS element maps for each nanorod generation. Cu $K\alpha$, Zn $K\alpha$, In $K\alpha$, Ga $K\alpha$, Co $K\alpha$, and Cd $L\alpha$ lines are shown in red, green, yellow, teal, purple, and blue respectively. **(C)** HRTEM image with overlaid EDS map highlighting the crystallinity of each material within the G-6 nanorod. **(D)** HRTEM image with overlaid EDS map for a G-2 ZnS–$Cu_{1.8}S$ nanorod and an enlarged part of the image showing the 1- to 2-nm structurally distinct interfacial region where the next exchange occurs **(E)** Experimental powder XRD pattern for the G-6 heterostructured nanorod, along with individual and combined simulated patterns that account for preferred orientation effects and the microscopically observed crystalline domain sizes. Reproduced with permission from ref. 85, Copyright 2020 The American Association for the Advancement of Science.

and predict which metals will incorporate into one another, providing a seemingly endless library of possible combinations which can be predicted by machine learning.[82]

Colloidal methods for incorporating several metal ions into a single particle can be achieved via cation exchange methods for metal oxide materials. Schaak and co-workers have devised schemes to incorporate up to 11 different cations into copper sulfide nanoparticles, all while preserving their colloidal stability and shape structures **(Figure 7)**. Copper sulfide nanoparticles can be mixed with divalent cations such as Zn^{2+}, Co^{2+}, and Cd^{2+} among others.[83] By doing so, mixed metal oxide domains are formed and redisperse in the particle to give varying architectures.[33] The formed different oxides can be selectively etched and further exchanged with other cations to expand the particle composition. For examples, rod structures with divets and truncations from the formed CdS domain being used as a template for AgS growth can be achieved.[84] Further, the different domains can be used as templates for Pd and Au growth to give plasmonic and photocatalytic responses. While
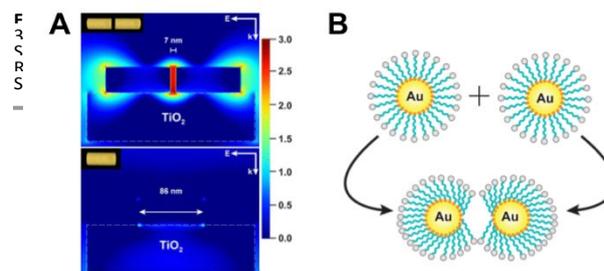
Journal Name CLE

Figure 9. Effects of dimerization on surface structure and plasmonics. **(A)** Plasmon enhancement of gold nanorods aligned end-to-end compared to single gold nanorods and nanospheres. Adapted with permission from ref. 89, Copyright 2014 American Chemical Society. **(B)** Dimerization of charged monolayer coated gold nanoparticles at close range. Reproduced with permission from ref. 93, Copyright 2013 American Chemical Society.

this gives extreme customizability in the type of material that could be made, due to the high entropy of the many-metal system, very little control on the position of the metals and the predictability of where they lie is available.[85]

Further control over the position of the metals is possible by co-reducing the desired metal ions onto the surface of a carefully selected seed particle. Skrabalak and co-workers have spent tremendous efforts optimizing syntheses based on this idea, coined the so-called seed-mediated co-reduction (SMCR).[86] While typically two metals are targeted total, meaning higher-order multimetal domains are not prevalent, there is stark control over the position of the metals on one another in solution. Using Au cores as seed particles, it is possible to control the pH and Pd concentration in the co-reduction step of more Au and Pd to yield particles with Au and Pd entirely separate or mixed into one phase. Utilizing the pH dependent kinetics of gold reduction by ascorbic acid, at fast reduction speed spiky gold particles form with terminal tips of Pd metal, and at slow reduction speeds a mixture material is formed with low energy facets (**Figure 8**).[87] The faceting of the seed particle and the relationship with the metal ions can control the final shape as well, giving multiple handles to controlling multimetallic particles. While the original demonstration of this system was conducted using metals processing comparable lattice constants, SMCR can also be applied to systems with a larger lattice mismatch between the depositing metals, albeit with more limited capacity to manipulate the metal distribution and ratios in the final nanoparticle products.[88]

4. Deterministic Assembly of Nanoparticles into "Polymers" and Well-Defined Structures

Site-selective functionalization can be used to direct NP assembly, with rational selection of ligands producing designer structures such as nanoclusters and "polymers" from NP "monomers." Just as NP morphology controls associated surface plasmon resonance (SPR), NPs' plasmonic properties are also altered by grouping behavior and interparticle distance, leading to the formation of "hot spots" **(Figure 9A).**[89,90] Our group recently showed that the alignment of gold nanospheres

(AuNSs) on graphene wrinkles pushes the SPR into the near-infrared range. This phenomenon is caused by longitudinal coupling of dipoles between AuNSs, and is extended as particles are confined in long columns on the graphene surface.[91] Plasmonic enhancement is especially useful in electronic and sensing applications and use of surface ligands has been explored as another method to control NP assembly off templates.[92] For example, Van Lehn and co-workers model the self-assembly of 5 nm AuNSs and demonstrate that thiol-coated AuNSs in particular may aggregate due to interactions between hydrophobic ligands (**Figure 9B**). This study used AuNSs coated with long alkane-thiols with charged end groups to allow for water-solubility and stability, and closely simulate NPs used in biological applications. Because of the long carbon chain and small particle size, ligands can freely deform and the hydrophobic effect simultaneously favors interactions between ligands on particles.[93] In addition, surface functionalization can direct growth of new NPs on specific faces of the parent particle. The Schaak group demonstrated this principle by combining complex assembly of heterogeneous trimers with nanosphere formation in distinct isomers.[94] Functionalization can control many aspects of NP assembly, leading to the rational selection of ligands that produce designer nanoclusters. The Glotzer group has shown that rational design can be increasingly specific, even controlling the length and angle at which nanospheres with two different polymer tethers assemble.[95]

The power of ligand-mediated assembly is easily demonstrated by end-to-end linking of nanorods. Our group achieved this type of assembly by performing a ligand exchange with biotin-disulfide on AuNRs. In this system, biotin-disulfide
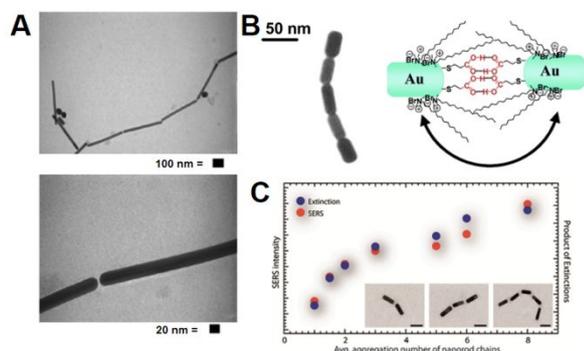
Figure 10. End-to-end assembly of nanorods. **(A)** End-to-end assembly of rods using biotin-streptavidin binding. Adapted with permission from ref. 96, Copyright 2003 American Chemical Society. **(B)** Linear assembly of gold nanorods in the presence of 3-mercaptopropionic acid. Adapted with permission from ref. 97, Copyright 2004 American Chemical Society. **(C)** Correlation between increase in SERS intensity and length of nanorod chain. Reproduced from ref. 101, Copyright 2011 American Chemical Society.

preferentially displaced the stabilizing surfactant (CTAB) at the ends of AuNRs rather than the lateral sides due to the difference in CTAB density at the ends. The selective functionalization of biotin-disulfide at the ends of NRs allowed us to link the biotin-AuNRs into long NP chains by leveraging the well-known binding interaction between biotin and streptavidin, which acts as a linker molecule (**Figure 10A**).[96] Nanoparticle "polymers" have also been prepared by utilizing hydrogen-bonding interaction between end-functionalized ligands such as 3-mercaptopropianic acid, which allows for the directed assembly of NRs without the need of an additional linker molecule (**Figure 10B**).[97] Furthermore, SAMs have been used to selectively functionalize one, two, or four faces of silver nanocubes (AgNCs) to induce specific arrangements of particles. AgNCs having one face coated with octadecanethiol (ODT) formed dimers, while AgNCs with two ODT faces that are opposite each other formed short chains. In this case, Xia and co-workers achieved face-selectivity by depositing particles onto a silica substrate and functionalizing the exposed faces with a hydrophilic SAM, followed by the removal of AgNCs from the substrate to coat the remaining faces with ODT. While throughput is limited by the size of the substrate, this approach allows anisotropic modifications on isotropic particles.[98] Kumacheva and co-workers report that polymers as surface ligands are also useful at establishing longer-range linkages between both NRs and NCs.[99,100] AuNRs exposed to a thiol-terminated polymer (polystyrene-SH) show preferential coating of the polymer at the ends, allowing AuNRs to assemble into chains or bundled-chains, depending on the concentration and molecular weight of polystyrene-SH.[99] For self-assembled strings of nanocubes (n=3), SERS enhancement increased by more than 200-fold, and nanospheres (n=4), SERS was enhanced by more than 100-fold.[100] Self-assembled NRs also follow this trend, and further show a correlation between increase in SERS and extinction (**Figure 10C**).[101] The distance between NRs can be regulated by ligand size.[99] While some work has been done on the study of SERS on NRs on substrates,[89] more work can be done to understand the effects of ligand size on interparticle distance and SERS hotspots in solution.

5. Molecular Stripes, Patches, and Altered Ligand Densities on Nanoparticles' Surfaces

The ability to tune the density or surface arrangement of ligands on NPs' surface gives NPs diverse functionalities and applications, especially when multiple ligand species of different properties are efficiently grafted to the NPs' surface. Mixtures of ligand molecules have been reported to form either by self-assembly or by using external templates and can adopt a random arrangement, form full (Janus) or partial (patchy/striped) phase segregation patterns **(Figure 11)**. While Janus mixed-ligand monolayers are mainly achieved via "stepwise" method where the ligands are introduced one at a time via masking methods discussed in Section 2; patchy/striped mixed ligands are often achieved by introducing

the ligands simultaneously at some ratio either during or post particle synthesis. Despite the importance of understanding how the ligands spatially distribute on the NPs' surface since it will determine how NPs interact with their environment,[102] there is no straightforward experimental characterization method to date for the mixed-ligand NPs.[103] The development of a characterization method to get a detailed picture of the self-organization of the mixed-ligands at the NPs' surface could pave the way for the ability to "paint" NPs with controllable molecular "colors," or the preparation of NPs with well-controlled ligands giving well-defined structural and biophysiochemical properties. Especially when the arrangement of ligands on NPs surface in mixed-ligands systems have been shown to influence cellular uptake, where only the NPs with specific relative position of different chemical functionalities would be able to directly pass-through cell membranes in an energy-independent way without causing membrane damage.[104] In addition, the specific arrangement of mixed-ligand systems has been shown to influence NPs' catalytic effect on the esterification of carboxylic acid reactions.[35]

5.1. Stripey Functionalization of Nanoparticles by Thiol Ligands
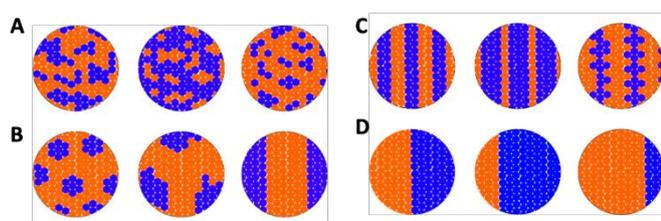
Figure 11. Illustrations of possible mixed-ligands arrangements on nanoparticles, including **(A)** random, **(B)** patchy, **(C)** striped, and **(D)** Janus-like compositions.

One of the current employed methods to characterizing the mixed-ligand monolayers on NPs is direct probing by Scanning Tunnelling Microscopy (STM) as demonstrated by Stellacci and co-workers,[104,105] where they presented STM images with ordered domains that were interpreted as parallel stripe-like patterns circling around the AuNS cores with tunable shape and size by varying the composition of ligand mixtures (**Figure 12A**). This body of work has been a source of much debate of whether the images reflect actual molecular positions, since obtaining high-resolution STM images is complex, requiring clean, monolayer sample besides the delicate instrumental settings.[106–109] NMR is an emerging method to indirectly probe ligand morphology, which provides surface morphology information since the chemical shift of nuclei is sensitive to their local ligand environment on the NPs' surface. Pradhan *et al.* take advantage of Nuclear Overhauser Effect Spectroscopy (NOESY) that allows estimation of the internuclear distance to assess the distribution of mixed-ligands on particles, where they found clear difference between randomly mixed monolayer NPs and Janus-like NPs coated with hexanethiolate and 2-(2-mercaptoethoxy)ethanol.[110] Stellacci and co-workers also employed 1D and 2D NMR in addition to STM to distinguish between random, stripe-like, and Janus-like morphologies of the mixed ligands on the NPs surface. NMR, however, is

hindered by the slow tumble of NPs due to their size, resulting in lower signals and broader peaks for bound molecules than for free molecules, demands for highly concentrated samples and longer collection times.[102] Besides further developing methods to improve mixed-ligand systems analysis via STM,[111] Stellacci and co-workers also utilized complementary techniques such as Fourier-transform infrared spectroscopy (FTIR),[112] atomic force microscopy (AFM),[113] and small angle neutron scattering (SANS)[114,115] to demonstrate the formation of stripe-like domains on NPs surface, which is suggested to be driven by entropic gain upon ligand separation by Glotzer and co-workers through molecular dynamics simulations.[116] Ge *et al.* used atomistic discrete molecular dynamics simulations to clarify the ongoing debate regarding the feasibility and origin of the striped pattern formation on NPs, where they found that stripe-like pattern could only emerge for a subset of binary self-assembled monolayer systems, and that this formation is also strongly dependent on the physicochemical characteristics of composite ligands.[117]

5.2. Nanoparticle Surface Patterning with Polymers

Phase separation in mixed polymer brushes is reported by Kumacheva and co-workers. By varying the molar ratio between the incompatible polystyrene (PS) and poly(ethylene glycol) (PEG), they generated a range of surface patterns, but most interestingly is helicoidal pattern of polystyrene patches wrapping around AuNRs. In contrast to the formation of patches in the case of homopolymer, where a thick uniform polymer brush breaks up into discrete number of pinned micelles upon reduction in solvent quality,[118] the gaps between the PS patches are filled with the second polymer (PEG), hence, arranging themselves into a helicoidal pattern on the AuNR surface as seen by TEM micrographs(**Figure 12B-D**).[119]
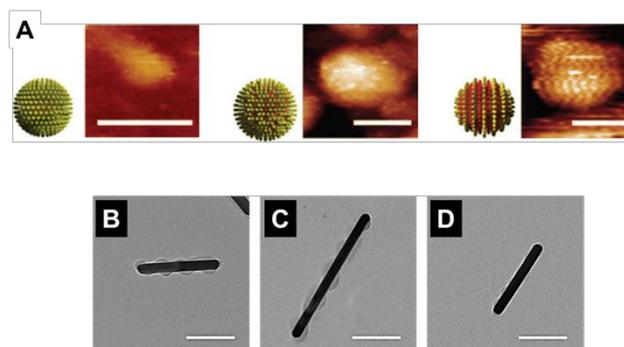

Figure 12. Examples of molecular stripes/patches on nanoparticles surfaces. **(A)** Schematics diagrams and representative STM images for homogenous **(left)**, random **(middle)**, and striped **(right)** monolayer organization of mixed-ligand shell. Scale bars are 5 nm. Adapted with permission from ref. 104, Copyright 2008 Springer Nature. **(B-D)** TEM images of AuNRs functionalized with **(B)** SH-PS-50K/SH-mPEG-10K, **(C)** SH-PS-50K/SH-mPEG-20K, and **(D)** SH-PS-20K/SH-mPEG-5K at 1:1 PS:PEG. Scale bars are 100 nm. Adapted with permission from ref. 119, Copyright 2019 American Chemical Society.

5.3. Characterization of Lipid Coatings on Inorganic Nanoparticles

Another class of ligands that holds potential for the surface patterning of (inorganic) nanoparticles is lipids. Coating inorganic nanoparticles with lipid bilayers has been shown to decrease their cytotoxicity and increase their stability in biological environments by effectively making them more "cell-like".[120] Typically, lipid coatings on inorganic nanoparticles take the form of 1) supported lipid bilayers in which the inner and outer leaflets both contain lipids or 2) hybrid lipid bilayers in which the inner leaflet contains an anchoring molecule such as an alkanethiol and lipids are found only in the outer leaflet.[120] Interestingly, it has been shown that gold nanoparticles (AuNPs) coated by a supported lipid bilayer are susceptible to fast etching by potassium cyanide, while those coated by a hybrid lipid bilayer of the same lipid composition can be stable in the presence of potassium cyanide for weeks.[121,122] This suggests that supported lipid bilayers are more permeable to cyanide ions and perhaps less closely/uniformly packed than, hybrid lipid bilayers which are able to more effectively prevent penetration of cyanide ions to the AuNP core. In fact, the degree of bilayer permeability can be fine-tuned by adjusting the amount of alkane thiol added to the AuNP-lipid mixture during the coating process.[122]
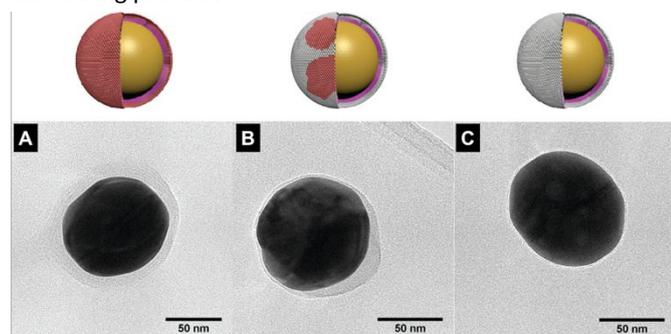
Figure 13. TEM images 90 nm OsO₄-stained C₁₈SH-functionalized AuNSs with lipid coatings containing (A) POPs alone, (B) a mixture of POPS and LPC (1:1), and (C) LPC alone. Only in the cases of 1:1 POPS:LPC are asymmetric coatings observed. Adapted with permission from ref. 121, Copyright 2012 American Chemical Society.

Separation of mixed lipid systems into liquid ordered and liquid disordered phases is well documented for supported lipid bilayers and synthetic giant unilamellar vesicles using approaches such as confocal fluorescence microscopy, fluorescence correlation spectroscopy, and atomic force microscopy.[123–125] Importantly, lipid phase separation and raft formation can also be observed in whole giant plasma membrane vesicles isolated from biological samples.[126] However, characterization of lipid phase separation on the surface of much smaller inorganic nanoparticles is more challenging to achieve by these techniques due to limited resolution and optical interference of certain core materials. To overcome these hurdles, our laboratory leveraged the preferential reaction of osmium tetroxide (OsO₄) with the double bonds in unsaturated lipid tails to selectively stain 1-palmitoyl-2-oleoyl-sn-glycero-3-phospho-L-serine (sodium salt) (POPS) molecules for visualization by TEM while leaving saturated 1-palmitoyl-2-hydroxy-sn-glycero-3-phosphocholine (LPC) molecules unstained. For both 50 nm and 90 nm AuNSs coated with a 1:1 ratio of POPS and LPC, asymmetric patches of stained organic material were observed on the NP surface

indicating the formation of POPS-rich domains (**Figure 13**). However, on smaller 20 nm AuNSs the same 1:1 ratio of POPS and LPC yielded a more uniform staining which surrounded the entire NS suggesting that on surfaces of higher curvature domain formation does not occur but rather POPS and LPC molecules remain equally distributed across the particle surface. We further showed that lipid domains on large 90nm particles could be tailored through the incorporation of functionalized lipid molecules to achieve targeted binding to desired substrates.[121]

More recently, Liu *et al.* reported patchy lipid surface chemistry for NP cores of various compositions when coated with cell-derived membrane materials through sonication or co-extrusion approaches.[127] By first functionalizing silica cores with fluorescent nitro-2,1,3-benzoxadiazol-4-yl (NBD) before coating with cell-derived membrane materials, Liu *et al*. were able to subsequently assess membrane coating integrity through the addition of a membrane impermeant fluorescence quencher, dithionite (DT) (**Figure 14A)**. While the fluorescence of fully coated silica particles was retained upon addition of DT, that of uncoated or partially coated particles was lost leading to a rapid drop in overall sample fluorescence that revealed up to 90% of particles possessed incomplete surface coatings (**Figure 14B)**. Patchy membrane coverage was further confirmed through negatively stained TEM imaging to be the dominant
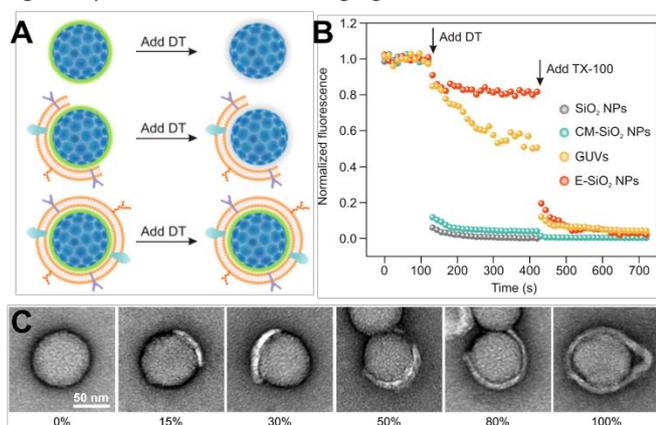
Figure 14. Characterization of incomplete cell membrane material coverage on the surface of silica nanoparticles. **(A)** Schematic representation of cell membrane material coating integrity assay in which dithionite (DT) is used to quench the fluorescence of nitro-2,1,3-benzoxadiazol-4-yl (NBD) on particles with incomplete coatings, **(B)** Representative fluorescence traces obtained from coating integrity assays for uncoated silica nanoparticles (grey), cell membrane-coated silica nanoparticles (teal), giant unilamellar vesicles (yellow), and endocytosed uncoated silica nanoparticles (red). DT was first added to bleach the fluorescence of particles with incomplete membrane coatings. Then, 1% Triton X-100 (TX-100) was added to disrupt intact membrane coatings and bleach the remaining fluorescence of fully coated particles, **(C)** TEM images of partially membrane-coated silica nanoparticles that have been negatively stained with uranyl acetate. Adapted from ref. 127, Copyright 2021 Springer Nature.

presentation for membrane-coated silica particles (**Figure 14C)** as well as various other membrane-coated core materials (i.e., magnetite, metal organic framework, gold, polymer, silica, and porous silicon). These results are in contrast with the popular assumption that such biomimetic particles possess uniform membrane coatings covering the entirety of the particle surface and have important implications for biomedical applications. In fact, Liu *et al*. showed through a combination of experimental and theoretical studies that particles possessing >50% membrane coating can be internalized by cells individually, while particles with <50% membrane coating must first form aggregates before entering the cell. Incomplete membrane coating can also impact biomolecular adsorption dynamics and cause premature leakage of cargo from drug delivery platforms. This makes more careful evaluation of membrane coating integrity an important consideration for the optimization of such biomimetic particles for biomedical applications.

5.4. Characterization of Ligand Density on the Nanoparticle Surface

As mentioned previously, NMR has great potential to characterize the ligands on the surface of NPs in solution; however, this technique has been largely limited to isotropic spherical NPs with diameters less than 6 nm. In order to expand on this approach, our lab investigated a series of AuNSs (1.2 to 25 nm) and AuNRs (aspect ratio 1.4 to 3.9) coated with (16-mercaptohexadecyl)-trimethylammonium bromide (MTAB). This system was chosen because MTAB particles are stable in aqueous solution at high concentration and the solvent-exposed proton of interest in the trimethylammonium headgroup is expected to suffer less line broadening than protons closer to the particle surface. Our NMR results show that MTAB coatings on AuNRs are isotropic, whereas MTAB ligand density varies with AuNSs diameter, with the smallest particles have the highest ligand densities despite having the most headgroup mobility. Combining NMR results with molecular dynamics (MD) simulations, we elucidated that the headgroup packing limits the ligand density rather than the sulfur packing on the NP surface, for ~10 nm or larger particles.[128] Scanning/transmission electron microscopy (S/TEM) is a routine characterization tool to measure the size, shape, and elemental composition of NP cores. Discerning ligand molecules and ligand morphology, however, is challenging since the ligand shell is often invisible under the electron beam. Although the use of stains,[121,127] or monolayer graphene as supporting film and low accelerating voltage in an aberration-corrected TEM can allow for direct visualization of ligand shells.[129] Electron energy loss spectroscopy (EELS) is an extremely powerful characterization tool, complementary to energy dispersive X-ray spectroscopy (EDX or EDS), in the STEM. While EDS is quite easy to use, it primarily excels at identifying atomic composition of heavier elements. On the other hand, EELS is historically known to be a difficult technique but can provide information on chemical bonding, optical properties, and vibrational modes in addition to spatially resolved atomic composition of low atomic number elements. EELS has seen great advancement in instrumentation developments, including monochromated electron sources, high resolution spectrometers, spherical aberration corrected electron probes, and electron detection sensors.[130] With the substantial improvements in resolution and signal-to-noise ratio of EELS technique, we have demonstrated the anisotropic distribution of the ligand molecules on NPs' surface via direct imaging using electron energy loss spectroscopy in an aberration-corrected scanning transmission electron microscopy (STEM-EELS).[60] We used carbon as the indicator of ligand density because of its higher abundance, higher stability under electron beam (compared to other elements such as N or S), and to take advantage of the 1-atom thick graphene substrate as a built-in standard for quantification of the carbon signal on an absolute scale. Our sample preparation and EELS method allows us to achieve the spatial resolution to detect subtle changes in ligand density for systems including CTAB-coated AuNRs (45 $\pm$ 5 nm x 15 $\pm$ 2 nm) and MTAB-coated AuNRs (31 $\pm$ 5 nm x 11 $\pm$ 1 nm). As seen in (**Figure 15)**, CTAB ligand density decreases locally at the ends of the NRs whereas MTAB ligand density is more uniform around the entire perimeter of the NRs.[60] These results

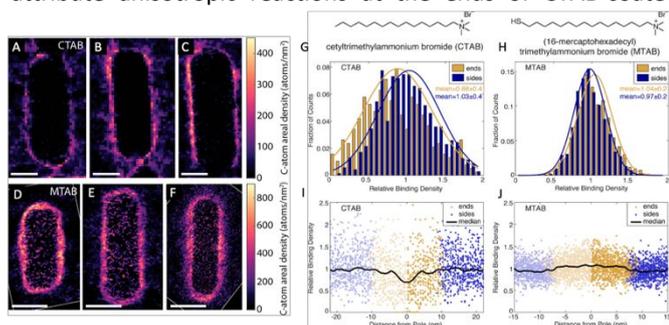support the hypotheses of previously discussed reports which attribute anisotropic reactions at the ends of CTAB-coated

Figure 15. ADF-STEM and ELLS spectral maps and quantification of variation in CTAB and MTAB distributions for multiple AuNRs . **(A-C)** Three EELS carbon compositional maps of CTAB-coated AuNRs with graphene background subtracted **(D-F)** Three EELS carbon compositional maps of MTAB-coated AuNRs with graphene background subtracted **(G,H)** Histogram of relative binding densities (ends in yellow, sides in blue) **(D,E)** plots of the profiles in both **(G)** and **(H)** include data for individual rod quarters (scatter plot) and a Savitzky-Golay filtered median (black line plot). In **(A-C)**, scale bars are 15 nm; in **(D-F)**, scale bars are 10 nm. Adapted from ref. 60, Copyright 2019 American Chemical Society. This is an unofficial adaptation from an article that appeared in an ACS publication. ACS has not endorsed the content of this adaptation or the context of its use.

AuNRs to decreased ligand density.[74,96,99,131] The improved EELS capability pioneers the quantification of carbon at sub-1-nm spatial resolution allowing us to show a 30% decrease in ligand density at the pole of the AuNRs coated with bilayer CTAB ligands,[132] whereas no changes in ligand density are observed for self-assembled monothiol MTAB coatings. Further investigations into the impact of nanorod dimensions and ligand identity are ongoing topics of interest in our lab.

6. Evaluation of the Present State of the Field and Future Directions

The ability to selectively functionalize different regions of colloidal nanoparticles allows for the preparation of nanomaterials with precise biophysiochemical properties. Selective functionalization can impart nanomaterials with unique morphologies and chemical identities that can regulate amphiphilicity, self-assembly, and selective interactions with proteins and other biological targets, enabling intentional design of engineered nanomaterials to interact with biological systems at the molecular level. As mentioned in this review, there have been great developments in nanoparticle synthesis that introduce controlled surface functionalization. Further expansion of these methods both for isotropic and anisotropic nanomaterials will be instrumental in advancing the field of metal nanomaterial synthesis, analogous to the field of small-molecule organic synthesis.

Developments of synthetic methodologies demand for development of new and advanced characterization techniques that allows for routine characterization of ligand shells. Currently, there is no straightforward experimental method to determine the ligand shell structure; although NMR and STEM-EELS show great potential for obtaining information on ligand arrangement and quantification on NPs, regardless of core material. In addition, *in situ* techniques that enable dynamic observation of the change in ligand shell structure as well as assembly in real time when NPs interact with biological entities or in a catalytic reaction is also desired. Especially when

establishing a direct translation between the intended, selective-functionalization and the actual biological effects remains a challenge. To this end, using a combination of experimental and theoretical approaches can provide insightful information in the physicochemical characteristics of the NPs before and after undergoing transformations in biological systems to fill the knowledge gap and establish a comprehensive framework to synthesize and characterize engineered nanomaterials with precise control over desired biological responses, catalytic, and electronic properties.

Author Contributions

All authors contributed to the writing of this article.

Khoi Nguyen L. Hoang is a Chemistry Ph.D. candidate in the Murphy Group at the University of Illinois Urbana-Champaign. She received her B.S. in Chemistry and Physics from Augsburg University in 2018. Her research interests include interactions and transformations of nanoparticles in the environment.

Sophia M. McClain is a Chemistry Ph.D. candidate and member of the Murphy Group at the University of Illinois Urbana-Champaign. She received her B.S. degree in Chemistry from Indiana University- Bloomington in 2018. Her research interests include modification of gold nanoparticle surface chemistry and subsequent study of gold nanoparticle/biomolecular interactions.

Sean M. Meyer obtained his doctorate in Chemistry from the Murphy Group at the University of Illinois Urbana-Champaign in 2022. He received his B.S. degree in Chemistry from Texas Tech University in 2017. His work mainly focuses on the use of plasmonic nanoparticles as SERS substrates and photothermal agents.

Catherine A. Jalomo is a Chemistry Ph.D. student and member of the Murphy and Zimmerman Groups at the University of Illinois, Urbana-Champaign. She received her B.S. degree in Chemistry from Fresno Pacific University in 2020. Her research focuses on nanoparticles for smart delivery systems.

Nathan B. Forney is a Chemistry Ph.D. student in the Murphy Group at the University of Illinois Urbana-Champaign. He received his B.S. in Chemistry and Biochemistry and Molecular Biology from Otterbein University in 2020. His research interests include quantitative EELS mapping of organic ligands on gold nanorods.

Catherine J. Murphy is the Larry R. Faulkner Endowed Chair in Chemistry at the University of Illinois Urbana-Champaign (UIUC). She earned B.S. degrees in chemistry and biochemistry from UIUC in 1986, and her Ph.D. in chemistry from the University of Wisconsin, Madison in 1990. She was a postdoctoral fellow at the California Institute of Technology from 1990-1993. From 1993-2009 she was on the faculty at the University of South Carolina. In 2009 she returned to UIUC as a faculty member.

ORCID IDs

Khoi Nguyen L. Hoang: 0000-0002-3822-4216
Sophia M. McClain: 0000-0003-4407-8080

Please do not adjust margins

ChemComm

Sean M. Meyer: 0000-0003-0771-5095
Catherine A. Jalomo: 0000-0002-1184-7405
Nathan B. Forney: 0000-0003-2652-0859
Catherine J. Murphy: 0000-0001-7066-5575

Conflicts of interest

There are no conflicts to declare.

Acknowledgements

References

1   S. E. Thompson and S. Parthasarathy, *Mater. Today*, 2006, **9**, 20–25.
2   Y. Liu, X. Duan, H. J. Shin, S. Park, Y. Huang and X. Duan, *Nature*, 2021, **591**, 43–53.
3   Apple unveils M2 with breakthrough performance and capabilities, https://www.apple.com/newsroom/2022/06/apple-unveils-m2-with-breakthrough-performance-and-capabilities/, (accessed 13 June 2022).
4   IBM Unveils World's First 2 Nanometer Chip Technology, Opening a New Frontier for Semiconductors, https://newsroom.ibm.com/2021-05-06-IBM-Unveils-Worlds-First-2-Nanometer-Chip-Technology,-Opening-a-New-Frontier-for-Semiconductors, (accessed 13 June 2022).
5   T. B. Hook, *Joule*, 2018, **2**, 1–4.
6   S. M. Dizaj, S. Vazifehasl, S. Salatin, K. Adibkia and Y. Javadzadeh, *Res. Pharm. Sci.*, 2015, **10**, 95–108.
7   A. Sparreboom, C. D. Scripture, V. Trieu, P. J. Williams, T. De, A. Yang, B. Beals, W. D. Figg, M. Hawkins and N. Desai, *Clin. Cancer Res.*, 2005, **11**, 4136–4143.
8   N. Desai, in *Albumin in Medicine: Pathogloical and Clinical Applications*, eds. M. Otagiri and V. T. Giam Chuang, Springer, Singapore, 2016, pp. 101–119.
9   P. Foroozandeh and A. A. Aziz, *Nanoscale Res. Lett.*, 2018, **13**, 339.
10 B. D. Chithrani, A. A. Ghazani and W. C. W. Chan, *Nano Lett.*, 2006, **6**, 662–668.
11 B. D. Chithrani and W. C. W. Chan, *Nano Lett.*, 2007, **7**, 1542–1550.
12 F. Lu, S. H. Wu, Y. Hung and C. Y. Mou, *Small*, 2009, **5**, 1408–1413.
13 F. Osaki, T. Kanamori, S. Sando, T. Sera and Y. Aoyama, *J. Am. Chem. Soc.*, 2004, **126**, 6520–6521.
14 M. Wu, H. Guo, L. Liu, Y. Liu and L. Xie, *Int. J. Nanomedicine*, 2019, **14**, 4247–4259.
15 A. Xu, M. Yao, G. Xu, J. Ying, W. Ma, B. Li and Y. Jin, *Int. J. Nanomedicine*, 2012, **7**, 3547–3554.
16 M. Zhu, G. Nie, H. Meng, T. Xia, A. Nel and Y. Zhao, *Acc. Chem. Res.*, 2013, **46**, 622–631.
17 S. C. Dunn, B. P. von der Heyden, A. Rozendaal and R. Taljaard, *Ore Geol. Rev.*, 2019, **107**, 87–107.
18 K. L. Kelly, E. Coronado, L. L. Zhao and G. C. Schatz, *J. Phys. Chem. B*, 2003, **107**, 668–677.
19 C. Burda, X. Chen, R. Narayanan and M. A. El-Sayed, *Chem. Rev.*, 2005, **105**, 1025–1102.
20 A. Sanchez, S. Abbet, U. Heiz, W. D. Schneider, H. Häkkinen, R. N. Barnett and U. Landman, *J. Phys. Chem. A*, 1999, **103**, 9573–9578.
21 M. H. Naveen, R. Khan and J. H. Bang, *Chem. Mater.*, 2021, **33**, 7595–7612.
22 C. N. Loynachan, A. P. Soleimany, J. S. Dudani, Y. Lin, A. Najer, A. Bekdemir, Q. Chen, S. N. Bhatia and M. M. Stevens, *Nat. Nanotechnol.*, 2019, **14**, 883–890.
23 J. G. Hinman, A. J. Stork, J. A. Varnell, A. A. Gewirth and C. J. Murphy, *Faraday Discuss.*, 2016, **191**, 9–33.
24 M. Quintanilla, C. Kuttner, J. D. Smith, A. Seifert, S. E. Skrabalak and L. M. Liz-Marzán, *Nanoscale*, 2019, **11**, 19561–19570.
25 J. Piella, N. G. Bastús and V. Puntes, *Chem. Mater.*, 2016, **28**, 1066–1075.
26 J. J. Velázquez-Salazar, L. Bazán-Díaz, Q. Zhang, R. Mendoza-Cruz, L. Montaño-Priede, G. Guisbiers, N. Large, S. Link and M. José-Yacamán, *ACS Nano*, 2019, **13**, 10113–10128.
27 M. Jin, H. Liu, H. Zhang, Z. Xie, J. Liu and Y. Xia, *Nano Res.*, 2011, **4**, 83–91.
28 B. J. Wiley, Y. Xiong, Z. Y. Li, Y. Yin and Y. Xia, *Nano Lett.*, 2006, **6**, 765–768.
29 Y. Sun and Y. Xia, *Science (80-.).*, 2002, **298**, 2176–2179.
30 H. C. Peng, S. Xie, J. Park, X. Xia and Y. Xia, *J. Am. Chem. Soc.*, 2013, **135**, 3780–3783.
31 J. S. Duchene, W. Niu, J. M. Abendroth, Q. Sun, W. Zhao, F. Huo and W. D. Wei, *Chem. Mater.*, 2013, **25**, 1392–1399.
32 M. H. Kim, S. K. Kwak, S. H. Im, J. B. Lee, K. Y. Choi and D. J. Byun, *J. Mater. Chem. C*, 2014, **2**, 6165–6170.
33 J. L. Fenton, B. C. Steimle and R. E. Schaak, *J. Am. Chem. Soc.*, 2018, **140**, 6771–6775.
34 B. Sadtler, D. O. Demchenko, H. Zheng, S. M. Hughes, M. G. Merkle, U. Dahmen, L. W. Wang and A. P. Alivisatos, *J. Am. Chem. Soc.*, 2009, **131**, 5285–5293.
35 A. Ghosh, S. Basak, B. H. Wunsch, R. Kumar and F. Stellacci, *Angew. Chemie - Int. Ed.*, 2011, **50**, 7900–7905.
36 C. Xie, Z. Niu, D. Kim, M. Li and P. Yang, *Chem. Rev.*, 2020, **120**, 1184–1249.
37 L. Nadav, O. R. Tsion and Z. Offer, *Talanta*, 2020, **208**, 120370.
38 C. Lu, L. Han, J. Wang, J. Wan, G. Song and J. Rao, *Chem.*

Please do not adjust margins

Soc. Rev., 2021, **50**, 8102–8146.

39   E. S. Cho, J. Kim, B. Tejerina, T. M. Hermans, H. Jiang, H. Nakanishi, M. Yu, A. Z. Patashinski, S. C. Glotzer, F. Stellacci and B. A. Grzybowski, *Nat. Mater.*, 2012, **11**, 978–985.

40   N. Osman, N. Devnarain, C. A. Omolo, V. Fasiku, Y. Jaglal and T. Govender, *Wiley Interdiscip. Rev. Nanomedicine Nanobiotechnology*, 2022, **14**, 1–24.

41   M. I. Khan, M. I. Hossain, M. K. Hossain, M. H. K. Rubel, K. M. Hossain, A. M. U. B. Mahfuz and M. I. Anik, *ACS Appl. Bio Mater.*, 2022, **5**, 971–1012.

42   Y. Du, W. Wei, X. Zhang and Y. Li, *J. Phys. Chem. C*, 2018, **122**, 7997–8002.

43   A. Walther and A. H. E. Müller, *Soft Matter*, 2008, **4**, 663–668.

44   S. Jiang, Q. Chen, M. Tripathy, E. Luijten, K. S. Schweizer and S. Granick, *Adv. Mater.*, 2010, **22**, 1060–1071.

45   C. Casagrande and M. Veyssié, *C. R. Acad. Sc. Paris*, 1988, **306**, 1423–1425.

46   C. Casagrande, P. Fabre, E. Raphaël and M. Veyssié, *EPL*, 1989, **9**, 251–255.

47   J. Zhang, B. A. Grzybowski and S. Granick, *Langmuir*, 2017, **33**, 6964–6977.

48   K. B. Shepard, D. A. Christie, C. L. Sosa, C. B. Arnold and R. D. Priestley, *Appl. Phys. Lett.*, , DOI:10.1063/1.4913913.

49   H. Liang, A. Cacciuto, E. Luijter and S. Granick, *Nano Lett.*, 2006, **6**, 2510–2514.

50   O. Shemi and M. J. Solomon, *Langmuir*, 2014, **30**, 15408–15415.

51   K. Nakahama, H. Kawaguchi and K. Fujimoto, *Langmuir*, 2000, **16**, 7882–7886.

52   L. Hong, S. Jiang and S. Granick, *Langmuir*, 2006, **22**, 9495–9499.

53   H. Gu, Z. Yang, J. Gao, C. K. Chang and B. Xu, *J. Am. Chem. Soc.*, 2005, **127**, 34–35.

54   W. Xu, J. Jia, T. Wang, C. Li, B. He, J. Zong, Y. Wang, H. J. Fan, H. Xu, Y. Feng and H. Chen, *Angew. Chemie - Int. Ed.*, 2020, **59**, 22246–22251.

55   Q. Li, E. Hu, K. Yu, R. Xie, F. Lu, B. Lu, R. Bao, T. Zhao, F. Dai and G. Lan, *Adv. Funct. Mater.*, 2020, **30**, 2004153.

56   A. Espinosa, J. Reguera, A. Curcio, Á. Muñoz-Noval, C. Kuttner, A. Van de Walle, L. M. Liz-Marzán and C. Wilhelm, *Small*, 2020, **16**, 1–14.

57   H. Xie, Z. G. She, S. Wang, G. Sharma and J. W. Smith, *Langmuir*, 2012, **28**, 4459–4463.

58   U. Aslam, S. Chavez and S. Linic, *Nat. Nanotechnol.*, 2017, **12**, 1000–1005.

59   R. Ghosh Chaudhuri and S. Paria, *Chem. Rev.*, 2012, **112**, 2373–2433.

60   B. E. Janicek, J. G. Hinman, J. J. Hinman, S. H. Bae, M. Wu, J. Turner, H. H. Chang, E. Park, R. Lawless, K. S. Suslick, C. J. Murphy and P. Y. Huang, *Nano Lett.*, 2019, **19**, 6308–6314.

61   M. J. Walsh, W. Tong, H. Katz-Boon, P. Mulvaney, J. Etheridge and A. M. Funston, *Acc. Chem. Res.*, 2017, **50**, 2925–2935.

62   F. Wang, S. Cheng, Z. Bao and J. Wang, *Angew. Chemie - Int. Ed.*, 2013, **52**, 10344–10348.

63   J. Reguera, J. Langer, D. Jiménez De Aberasturi and L. M.

64   S. M. Meyer and C. J. Murphy, *Nanoscale*, 2022, **14**, 5214–5226.

65   N. S. Abadeer, M. R. Brennan, W. L. Wilson and C. J. Murphy, *ACS Nano*, 2014, **8**, 8392–8406.

66   S. Lee, L. J. E. Anderson, C. M. Payne and J. H. Hafner, *Langmuir*, 2011, **27**, 14748–14756.

67   I. Gorelikov and N. Matsuura, *Nano Lett.*, 2008, **8**, 369–373.

68   S. M. Meyer and C. J. Murphy, *Nanoscale*, 2022, **14**, 5214–5226.

69   X. Zhu, H. Jia, X.-M. Zhu, S. Cheng, X. Zhuo, F. Qin, Z. Yang and J. Wang, *Adv. Funct. Mater.*, 2017, **27**, 1700016.

70   C. M. Huang, M. F. Chung, J. S. Souris and L. W. Lo, *APL Mater.*, , DOI:10.1063/1.4898415.

71   M. Adelt, D. A. Maclaren, D. J. S. Birch and Y. Chen, *ACS Appl. Nano Mater.*, 2021, **4**, 7730–7738.

72   M. Wang, A. Hoff, J. E. Doebler, S. R. Emory and Y. Bao, *Langmuir*, 2019, **35**, 16886–16892.

73   L. R. Rowe, B. S. Chapman and J. B. Tracy, *Chem. Mater.*, 2018, **30**, 6249–6258.

74   J. G. Hinman, J. R. Eller, W. Lin, J. Li, J. Li and C. J. Murphy, *J. Am. Chem. Soc.*, 2017, **139**, 9851–9854.

75   W. Ren, Y. Zhou, S. Wen, H. He, G. Lin, D. Liu and D. Jin, *Chem. Commun.*, 2018, **54**, 7183–7186.

76   B. Wu, D. Liu, S. Mubeen, T. T. Chuong, M. Moskovits and G. D. Stucky, *J. Am. Chem. Soc.*, 2016, **138**, 1114–1117.

77   H. Jia, A. Du, H. Zhang, J. Yang, R. Jiang, J. Wang and C. Y. Zhang, *J. Am. Chem. Soc.*, 2019, **141**, 5083–5086.

78   X. Yang, Y. Liu, S. H. Lam, J. Wang, S. Wen, C. Yam, L. Shao and J. Wang, *Nano Lett.*, 2021, **21**, 8205–8212.

79   J. W. Hong, D. H. Wi, S. U. Lee and S. W. Han, *J. Am. Chem. Soc.*, 2016, **138**, 15766–15773.

80   P.-C. Chen, X. Liu, J. L. Hedrick, Z. Xie, S. Wang, Q.-Y. Lin, M. C. Hersam, V. P. Dravid and C. A. Mirkin, *Science (80-.).*, 2016, **352**, 1565–1569.

81   P. C. Chen, M. Liu, J. S. Du, B. Meckes, S. Wang, H. Lin, V. P. Dravid, C. Wolverton and C. A. Mirkin, *Science (80-.).*, 2019, **363**, 959–964.

82   C. B. Wahl, M. Aykol, J. H. Swisher, J. H. Montoya, S. K. Suram and C. A. Mirkin, *Sci. Adv.*, 2021, **7**, 1–10.

83   J. L. Fenton, B. C. Steimle and R. E. Schaak, *Science (80-.).*, 2018, **360**, 513–517.

84   R. E. Schaak, B. C. Steimle and J. L. Fenton, *Acc. Chem. Res.*, 2020, **53**, 2558–2568.

85   B. C. Steimle, J. L. Fenton and R. E. Schaak, *Science (80-.).*, 2020, **367**, 418–424.

86   R. G. Weiner, M. R. Kunz and S. E. Skrabalak, *Acc. Chem. Res.*, 2015, **48**, 2688–2695.

87   C. J. Desantis, A. C. Sue, M. M. Bower and S. E. Skrabalak, *ACS Nano*, 2012, **6**, 2617–2628.

88   M. R. Kunz, S. M. McClain, D. P. Chen, K. M. Koczkur, R. G. Weiner and S. E. Skrabalak, *Nanoscale*, 2017, **9**, 7570–7576.

89   B. F. Mangelson, M. R. Jones, D. J. Park, C. M. Shade, G. C. Schatz and C. A. Mirkin, *Chem. Mater.*, 2014, **26**, 3818–3824.

90   M. G. Blaber and G. C. Schatz, *Chem. Commun.*, 2011, **47**,

Liz-Marzán, *Chem. Soc. Rev.*, 2017, **46**, 3866–3885.

3769–3771.

91   M. T. Gole, Z. Yin, M. C. Wang, W. Lin, Z. Zhou, J. Leem, S. Takekuma, C. J. Murphy and S. W. Nam, *Sci. Rep.*, 2021, **11**, 1–9.

92   G. Wu, J. Zhu, G. Weng, J. Li and J. Zhao, *Microchim. Acta*, 2021, **188**, 345.

93   R. C. Van Lehn and A. Alexander-Katz, *Langmuir*, 2013, **29**, 8788–8798.

94   J. M. Hodges and R. E. Schaak, *Acc. Chem. Res.*, 2017, **50**, 1433–1440.

95   C. R. Iacovella and S. C. Glotzer, *Nano Lett.*, 2009, **9**, 1206–1211.

96   K. K. Caswell, J. N. Wilson, U. H. F. Bunz and C. J. Murphy, *J. Am. Chem. Soc.*, 2003, **125**, 13914–13915.

97   K. G. Thomas, S. Barazzouk, B. I. Ipe, S. T. S. Joseph and P. V. Kamat, *J. Phys. Chem. B*, 2004, **108**, 13066–13068.

98   M. Rycenga, J. M. McLellan and Y. Xia, *Adv. Mater.*, 2008, **20**, 2416–2420.

99   Z. Nie, D. Fava, M. Rubinstein and E. Kumacheva, *J. Am. Chem. Soc.*, 2008, **130**, 3683–3689.

100   A. Klinkova, H. Thérien-Aubin, A. Ahmed, D. Nykypanchuk, R. M. Choueiri, B. Gagnon, A. Muntyanu, O. Gang, G. C. Walker and E. Kumacheva, *Nano Lett.*, 2014, **14**, 6314–6321.

101   A. Lee, G. F. S. Andrade, A. Ahmed, M. L. Souza, N. Coombs, E. Tumarkin, K. Liu, R. Gordon, A. G. Brolo and E. Kumacheva, *J. Am. Chem. Soc.*, 2011, **133**, 7563–7570.

102   N. D. Burrows, W. Lin, J. G. Hinman, J. M. Dennison, A. M. Vartanian, N. S. Abadeer, E. M. Grzincic, L. M. Jacob, J. Li and C. J. Murphy, *Langmuir*, 2016, **32**, 9905–9921.

103   P. Pengo, M. Şologan, L. Pasquato, F. Guida, S. Pacor, A. Tossi, F. Stellacci, D. Marson, S. Boccardo, S. Pricl and P. Posocco, *Eur. Biophys. J.*, 2017, **46**, 749–771.

104   A. Verma, O. Uzun, Y. Hu, Y. Hu, H. S. Han, N. Watson, S. Chen, D. J. Irvine and F. Stellacci, *Nat. Mater.*, 2008, **7**, 588–595.

105   A. M. Jackson, J. W. Myerson and F. Stellacci, *Nat. Mater.*, 2004, **3**, 330–336.

106   Y. Cesbron, C. P. Shaw, J. P. Birchall, P. Free and R. Lévy, *Small*, 2012, **8**, 3714–3719.

107   J. Stirling, I. Lekkas, A. Sweetman, P. Djuranovic, Q. Guo, B. Pauw, J. Granwehr, R. Lévy and P. Moriarty, *PLoS One*, 2014, **9**, e108482.

108   M. Yu and F. Stellacci, *Small*, 2012, **8**, 3720–3726.

109   Q. K. Ong and F. Stellacci, *PLoS One*, 2015, **10**, 1–19.

110   S. Pradhan, L. E. Brown, J. P. Konopelski and S. Chen, *J. Nanoparticle Res.*, 2009, **11**, 1895–1903.

111   Q. K. Ong, J. Reguera, P. J. Silva, M. Moglianetti, K. Harkness, M. Longobardi, K. S. Mali, C. Renner, S. De Feyter and F. Stellacci, *ACS Nano*, 2013, **7**, 8529–8539.

112   A. Centrone, Y. Hu, A. M. Jackson, G. Zerbi and F. Stellacci, *Small*, 2007, **3**, 814–817.

113   J. J. Kuna, K. Voïtchovsky, C. Singh, H. Jiang, S. Mwenifumbo, P. K. Ghorai, M. M. Stevens, S. C. Glotzer and F. Stellacci, *Nat. Mater.*, 2009, **8**, 837–842.

114   M. Moglianetti, Q. K. Ong, J. Reguera, K. M. Harkness, M. Mameli, A. Radulescu, J. Kohlbrecher, C. Jud, D. I. Svergun

115   Z. Luo, Y. Yang, A. Radulescu, J. Kohlbrecher, T. A. Darwish, Q. K. Ong, S. Guldin and F. Stellacci, *Chem. Mater.*, 2019, **31**, 6750–6758.

116   C. Singh, P. K. Ghorai, M. A. Horsch, A. M. Jackson, R. G. Larson, F. Stellacci and S. C. Glotzer, *Phys. Rev. Lett.*, 2007, **99**, 1–4.

117   X. Ge, P. C. Ke, T. P. Davis and F. Ding, *Small*, 2015, **11**, 4894–4899.

118   R. M. Choueiri, E. Galati, H. Thérien-Aubin, A. Klinkova, E. M. Larin, A. Querejeta-Fernández, L. Han, H. L. Xin, O. Gang, E. B. Zhulina, M. Rubinstein and E. Kumacheva, *Nature*, 2016, **538**, 79–83.

119   H. Tao, L. Chen, E. Galati, J. G. Manion, D. S. Seferos, E. B. Zhulina and E. Kumacheva, *Langmuir*, 2019, **35**, 15872–15879.

120   A. Luchini and G. Vitiello, *Front. Chem.*, 2019, **7**, 1–16.

121   J. A. Yang and C. J. Murphy, *Langmuir*, 2012, **28**, 5404–5416.

122   R. E. Messersmith, G. J. Nusz and S. M. Reed, *J. Phys. Chem. C*, 2013, **117**, 26725–26733.

123   K. Bacia, P. Schwille and T. Kurzchalia, *Proc. Natl. Acad. Sci. U. S. A.*, 2005, **102**, 3272–3277.

124   T. Sych, C. O. Gurdap, L. Wedemann and E. Sezgin, *Membranes (Basel).*, 2021, **11**, 323.

125   M. P. Mingeot-Leclercq, M. Deleu, R. Brasseur and Y. F. Dufrêne, *Nat. Protoc.*, 2008, **3**, 1654–1659.

126   E. Sezgin, H. J. Kaiser, T. Baumgart, P. Schwille, K. Simons and I. Levental, *Nat. Protoc.*, 2012, **7**, 1042–1051.

127   L. Liu, X. Bai, M. V. Martikainen, A. Kårlund, M. Roponen, W. Xu, G. Hu, E. Tasciotti and V. P. Lehto, *Nat. Commun.*, 2021, **12**, 1–12.

128   M. Wu, A. M. Vartanian, G. Chong, A. K. Pandiakumar, R. J. Hamers, R. Hernandez and C. J. Murphy, *J. Am. Chem. Soc.*, 2019, **141**, 4316–4327.

129   Z. Lee, K. J. Jeon, A. Dato, R. Erni, T. J. Richardson, M. Frenklach and V. Radmilovic, *Nano Lett.*, 2009, **9**, 3365–3369.

130   J. L. Hart, A. C. Lang, A. C. Leff, P. Longo, C. Trevor, R. D. Twesten and M. L. Taheri, *Sci. Rep.*, 2017, **7**, 1–14.

131   T. K. Sau and C. J. Murphy, *Langmuir*, 2005, **21**, 2923–2929.

132   B. Nikoobakht and M. A. El-Sayed, *Langmuir*, 2001, **17**, 6368–6374.

and F. Stellacci, *Chem. Sci.*, 2014, **5**, 1232–1240.